Contents

Contents **a**

1 Nucleation probability assessment - a phase field methodology **1**
1.1 Introduction 1
1.2 Simulated system 2
1.3 Some fundamentals 3
1.4 Methodology - domain scaling 4
1.5 Implementation of general Neumann BC 4
1.5.1 Tilted straight line 5
1.5.2 Examples 6
1.6 Proof-of-concept application 6

2 Analytic nucleation probability assessment and Monte Carlo simulations **7**
2.1 Introduction 7
2.1.1 Terminology in heterogeneous nucleation 8
2.1.2 Heterogeneous spatial nucleation and shape factor . . . 8
2.2 Nucleation probability assessment 11
2.2.1 Problem statement 11
2.2.2 Stability as function of the bottom grain orientation . . 13
2.2.3 Shape factor-orientation maps 13
2.3 Monte Carlo simulations 16
2.3.1 Algorithm description 16
2.3.2 Validation of anisotropic growth 20
2.3.3 Methodology 21
2.3.4 Results 23
2.4 Comparison to experiment and discussion 27
2.5 Conclusion 29

List of publications **33**

Chapter 1

Nucleation probability assessment - a phase field methodology

1.1 Introduction

This chapter develops a methodology to obtain insight about the nucleation barrier from the equilibrium shapes of particles with anisotropic interface energy obtained by phase field simulation. The used model represents wetting of a plane by a crystal and combines the features developed by the author: the inclination dependence of interface energy, volume conservation using the fictitious concentration field approach and the general Neumann boundary conditions to control the interface inclination at the domain boundary.

Advantage of the method is that it does not a-priori assume any shape, it is thus in principle usable for non-analytic cases, where the solution is not known.

The below procedure assumes a 2D particle sitting on top of a line, the contact angles on the left and right are known. It is assumed that the environment surrounding the particle is liquid and the particle-liquid energy is anisotropic. The contact angles are determined using the Young's equation.

The following sections describe how the phase field result can be used to bring insight about the nucleation barrier using scaling of simulation domain, which is a kind of post-processing of the results.

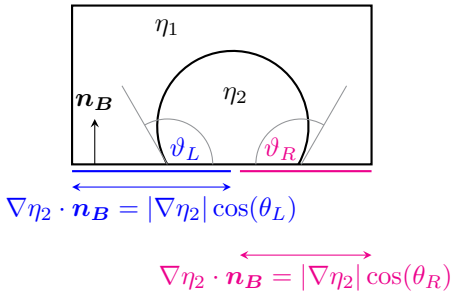

Figure 1.1: Sketch of the geometry in the phase-filed simulations used in the domain scaling methodology for nucleation barrier assessment. The symbols ϑ_L, ϑ_R denote tangent angles in the contact points and θ_L, θ_R the normal ones. The intervals on the bottom domain boundary with the different interface inclination imposed are indicated (note that η_1 has analogous boundary conditions which must be consistent).

1.2 Simulated system

Principle of the method is in utilizing the fact, that in the simulated geometry, the total energy of the system is in fact the particle-liquid interface energy.

The critical nucleation barrier is total energy change upon insertion of the critical nucleus. That is such nucleus, which just balances the bulk and interface energy contributions.

The phase field simulation provides the interface-energy-minimizing shape for the input contact angles

The simulated system geometry is sketched in Figure 1.1. A two-phase system of aparticle in a liquid was described by two phase field variables in Moelans' model, one representing the liquid parent phase (η_1) and the second (η_2) representing the particle (possibly with anisotropic interface energy). The bottom domain boundary then represents the substrate and the interface inclination in the two contact points is controlled by the boundary condition as indicated in the figure.

Volume conservation was assured using the fictitious concentration field.

1.3 Some fundamentals

In 2D, the Gibbs free energy difference upon a nucleus insertion in the system is due to competition between area and line energy contributions (see also Figure **??**b). Be A_{hom} the nucleus area and its interface be described by a parametric curve $\mathcal{C}$. In the isotropic case, $\mathcal{C}$ is a circle and the interfacial contribution is simply σL, where $L = 2\pi R$ is the interface length and σ the isotropic specific interface energy. The Gibbs free energy difference of a free nucleus is then (with ΔG_A being supersaturation)

$$\Delta G_{hom} = -\Delta G_A A_{hom} + \sigma L \tag{1.1}$$

$$= (-\Delta G_A R^2 + 2R\sigma)\pi\,, \tag{1.2}$$

which implies the critical radius

$$R_c = \frac{\sigma}{\Delta G_A} \tag{1.3}$$

and critical nucleation barrier

$$(\Delta G_c^*)_{hom} = \hat{A}_{hom}\frac{\sigma^2}{\Delta G_A}\,, \tag{1.4}$$

where the non-dimensional nucleus area is $\hat{A}_{hom} = A_{hom}/R^2 = \pi$.

In heterogeneous nucleation, the shape factor $S(\theta) = A_{het}/A_{hom}$ has equal role as in the 3D space, implying

$$\Delta G_{het} = S(\theta)\Delta G_{hom} \tag{1.5}$$

similarly as for the nucleation barrier

$$(\Delta G_c^*)_{het} = S(\theta)(\Delta G_c^*)_{hom}\,. \tag{1.6}$$

When the interface energy is inclination-dependent $\sigma(\theta) = \sigma_0 f(\theta)$, the interface energy contribution is a line integral $\int_{\mathcal{C}} \sigma(\theta)\mathrm{d}l$, which can be expressed in analogy with the 3D case [Mariaux2010] as (X_0 being the generalized radius of the Wulff shape with area A_{hom}^{ani})

$$\int_{\mathcal{C}} \sigma(\theta)\mathrm{d}l = \frac{2\sigma_0}{X_0}A_{hom}^{ani}\,, \tag{1.7}$$

which eventually allows to write the Gibbs free energy difference of a free nucleus

$$\Delta G_{hom}^{ani} = (-\Delta G_A X_0^2 + 2\sigma_0 X_0)\hat{A}_{hom}^{ani} \tag{1.8}$$

and further its nucleation barrier

$$(\Delta G_c^*)_{hom} = \hat{A}_{hom}^{ani} \frac{2\sigma^2}{\Delta G_A} \,. \tag{1.9}$$

In the heterogeneous anisotropic nucleation the difference in Gibbs free energy is like in equation (1.5), having ΔG_{hom}^{ani} as in (1.8) and the nucleation barrier like in (1.6), only with modified shape factor correspondingly to the Wulff shape.

b)

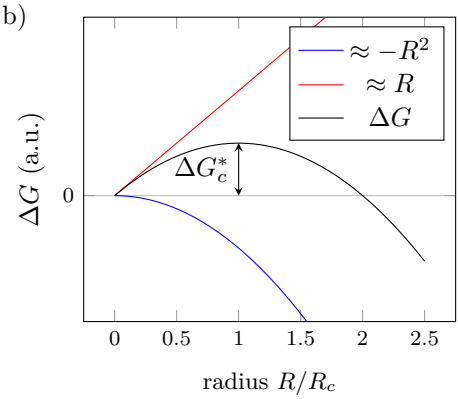

1.4 Methodology - domain scaling

The critical nucleation barrier is the maximal possible energy change attributed to insertion a nucleus of a particular shape, interface energy and in the present supersaturation (bulk driving force in general). In The Gibbs free energy change upon a nucleus insertion in 2D reads

1.5 Implementation of general Neumann BC

The Appendix **??** contains the necessary modifications to the finite-difference algorithm when implementing the general Neumann boundary conditions. Eventually, the changes affected all the finite difference operators (standing in place of unidirectional derivatives and laplacian), but only in the parts of the matrices, which interact with the domain boundary.

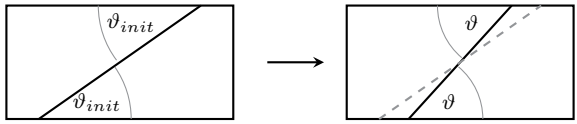

Figure 1.2: Validation of the general NBC for control of the inclination angle at the boundary - tilted line simulations (isotropic interface energy). In the simulations with inclination-dependent interface energy there was $\vartheta_{init} = \vartheta$

1.5.1 Tilted straight line

The implementation of general Neumann boundary conditions controlling the inclination angle at the domain boundary was validated in simulations sketched in Figure 1.2. A slightly different approach had to be taken in the case with isotropic and anisotropic interface energy, as described below.

In the case with isotropic interface energy, the initial condition for the simulation was a tilted line, which was inclined under different angle ϑ_{init} than the imposed inclination angle ϑ. The simulation ran until the total energy converged (i.e. until the change in energy per time step was smaller than a threshold). The final state was expected to be a line aligned under the target angle ϑ. From linear fit of the final phase field contour, the resulting inclination angle was read out. A range of angles between 15°-165°was probed, and the results were plotted in Figure 1.3a. As can be seen, a perfect match was achieved.

When validating the same with inclination-dependent interface energy, the methodology had to be modified slightly: the straight line was placed in its imposed position already in the initial condition, i.e. $\vartheta_{init} = \vartheta$. That was because once any curvature appeared in the straight line (which happened when the interface was forced to move by the boundary conditions), it began deforming and there remained no straight line. To assure that the tilted line be the equilibrium state of the system, the anisotropy function was always rotated so that the target inclination angle ϑ corresponded to the minimal interface energy. Only then the straight line could be immobile and the general Neumann BC could be validated in the same way like with the isotropic interface energy, i.e. simulation until energy convergence and linear fit of the contour. The target angle was observed very accurately in this case as well, as can be seen in Figure 1.3b.

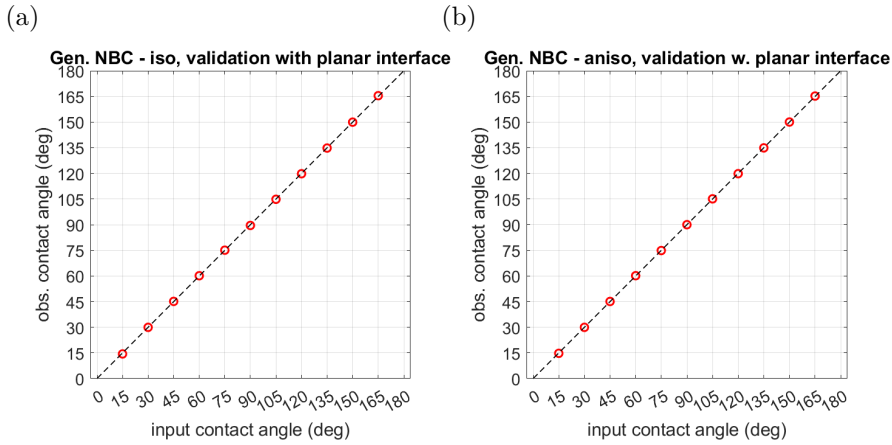

Figure 1.3: Results of tilted plane validation. In a) the result with isotropic interface, in b) with anisotropic one.

1.5.2 Examples

1.6 Proof-of-concept application

Chapter 2

Analytic nucleation probability assessment and Monte Carlo simulations

2.1 Introduction

The method developed in this paper obtains anisotropy in nucleation barrier (and, eventually, the nucleation probability) as function of the interface energy anisotropy, bottom grain orientation and the nucleus orientation. The method is based on principles of classical nucleation theory. Then, in order to demonstrate the effect of the anisotropic barrier on the film texture, a Monte Carlo algorithm was developed and used to simulate growth and nucleation in a polycrystalline film. The aim of this paper is to qualitatively explore the implications of the anisotropic interface energy for the orientation selection during repeated nucleation in the polycrystalline growth.

The paper is organized in five main parts. Firstly, the necessary fundamentals are described in Section **??** and some theoretical novelties regarding the Winterbottom construction are introduced. In Section 2.2, the problem specification defines all parameters in the orientation-dependent Winterbottom construction to be solved and successively the shape factor-orientation maps are presented and explained. These are used as input in the Monte Carlo simulations described in Section 2.3, together with their results. The Section 2.4 applies the obtained insights to a peculiar case of texture evolution in experiment [1]

(electrodeposited nickel). There, a sudden change in texture occurred after thickness of 2 µm, supposedly due to nucleation. The nucleation brought in new orientations, which succeeded in the growth competition. Interestingly, the said film was deposited very slowly, hence the high nucleation rate is rather unexpected when viewed in the perspective of classical nucleation theory with isotropic interface energy. However, with the anisotropic interface energy included as worked out here, a qualitative explanation was found.

2.1.1 Terminology in heterogeneous nucleation

3D nucleation and 2D nucleation are terms used in classical nucleation theory to describe two different nucleation mechanisms on a plane in 3D space.

In 3D nucleation, the nuclei form as 3D clusters on the flat substrate and their interface energy is derived mostly from their curved surface. The possible edge and vortex energies are usually neglected. The clusters grow and coalesce.

In 2D nucleation, the nucleus is a mono-atomic step (usually assumed in a shape of a disc) on the (theoretically) atomically smooth surface. In the total nucleus interface energy, the edge energy cannot be neglected. The nuclei grow along the surface layer by layer.

These concepts can be reduced to 2D space, where the 3D nucleation is equivalent to 2D nucleation and the 2D nucleation to 1D nucleation. In order to simplify the terminology when describing the results from 2D space, the terms spatial and interfacial nucleation are introduced, which indicate the difference in the mechanism irrespective of the used dimension.

This paper only deals with the anisotropy in nucleation barriers of nuclei created in *spatial* nucleation. That is because it is not expected that the grain orientation could change during the *interfacial* nucleation, which is essentially a locallized epitaxial growth. In the following, the *spatial nucleus* denotes a nucleus created in spatial nucleation.

2.1.2 Heterogeneous spatial nucleation and shape factor

Note that the formulas and their description in this section are given for 2D space, but they could easily be generalized to 3D.

Because nucleation is a thermally activated process, the probability P of finding the critical nucleus at a certain spot follows the Arrhenius relation

$$P \approx \exp\left(-\frac{\Delta G_c^*}{kT}\right) , \tag{2.1}$$

where k is the Boltzmann constant, T absolute temperature and ΔG_c^* is the *critical nucleation barrier* (in J), which is to be overcome by the thermal fluctuations in order to form a critical nucleus. A nucleus with the critical area A_c is metastable. The nucleation barrier ΔG_c^* is the *nucleation work* [7] to be done in order to insert a critical nucleus. Subcritical nuclei dissolve, the supercritical ones grow.

In heterogeneous nucleation (i.e. nucleation on a wall), a shape factor $S \geq 0$ is the ratio of the heterogeneous nucleus area A_{het} to the area of the isolated particle A_{hom} (homogenous nucleus) generated at equivalent conditions. It can thus be written as a proportionality factor

$$A_{het} = SA_{hom} . \tag{2.2}$$

The force balance of the meeting interfaces determines the wetting, which decides the value of S. When $S = 0$, no spatial nucleus (here 2D nucleus) is inserted, because complete wetting occurs and only interfacial (1D) nucleation is possible.

Because it was shown in [6], that the nucleation barrier is proportional to the actual area of the nucleus, the shape factor relates the nucleation barriers too, hence

$$\Delta G_{het}^* = S\Delta G_{hom}^* . \tag{2.3}$$

The above implies, that knowing the homogeneous nucleation barrier and the shape factor for a particular heterogeneous nucleus allows to determine the heterogeneous nucleation barrier and also the relative difference in nucleation probability. This reduces the problem of heterogeneous nucleation probability to the determination of a shape factor, obtained as ratio of areas of heterogeneous and homogeneous nucleus.

It should be emphasized, that in the case of multiple possible shape solutions (like e.g. in Figure **??**a), the Wulff shape of the first order (Figure **??**b) was always assumed as the homogeneous nucleus in the shape factor determination. That choice was made because the nucleation barrier is proportional to the inserted nucleus area (see (2.4)), which implies that smaller nuclei have larger nucleation probability. The Wulff shape of the first order is the smallest one, hence the most likely to occur.

In 2D, the critical homogeneous nucleation barrier $(\Delta G_c^*)_{hom}$ depends on the scalar interface energy σ_0 from $\sigma(\theta) = \sigma_0 h(\theta)$ (i.e. as in (**??**)) and the bulk driving force for the phase transformation ΔG_V as

$$(\Delta G_c^*)_{hom} = \hat{A}_{hom} \frac{\sigma_0^2}{\Delta G_V} \,. \tag{2.4}$$

where $\hat{A}_{hom} = A_{hom}/R^2$ is a non-dimensional area of the nucleus, R being a radius of the nucleus. If the nucleus is a particle with anisotropic interface energy, then R is a generalized radius, a scalar factor scaling the area of the particle. In classical nucleation theory in 2D (with both isotropic and anisotropic interface energy [6]) it is simply

$$R = \frac{\sigma_0}{\Delta G_V} \tag{2.5}$$

In order to get a reasonable nucleation rate of 1 $\mathrm{cm}^{-3}\mathrm{s}^{-1}$ and larger, the homogeneous nucleation barrier ought to be $(\Delta G_c^*)_{hom} \leq 78\,kT$, but at the same time it should be $(\Delta G_c^*)_{hom} \geq 10\,kT$, because the nucleus radius then gets so small, that the applicability of the continuous approach of classical nucleation theory becomes questionable [11, pp.195].

Let the symbol

$$\beta = \hat{A}_{hom} \frac{\sigma_0^2}{\Delta G_V} \frac{1}{kT} \tag{2.6}$$

stand for the non-dimensional nucleation barrier, i.e. the nucleation barrier expressed in multiples of kT. Apparently, $10 \leq \beta \leq 78$, in order to observe a reasonable amount of nucleation describable by classical nucleation theory. Then, the homogeneous nucleation probability can be written as

$$P_{hom} = \omega \exp(-\beta) \tag{2.7}$$

and the heterogeneous one

$$P_{het} = \omega \exp(-\beta S) \,. \tag{2.8}$$

The vibration frequency ω represents the number of nucleation attempts per unit of time (assumed to be a constant in this paper).

Note that β aggregates information about temperature, the driving force and the interface energy. In this paper, the temperature T and σ_0 are assumed to be constant. Consequently, when β varies, the bulk driving force ΔG_V is varied inversely, as can be seen from the equation (2.6). This way, the variations in β are also related to the deposition rate, because the higher the driving force, the higher the deposition rate.

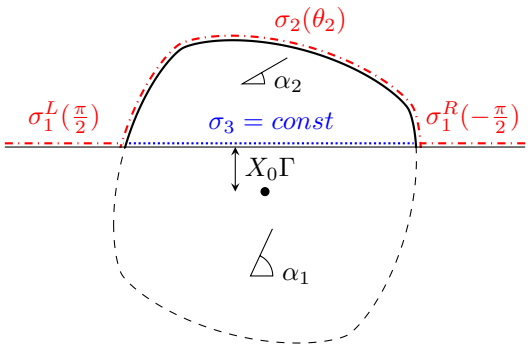

Figure 2.1: Winterbottom construction on a weak-anisotropy Wulff shape with indication of the distinct types of interfaces: red and dash-dotted line is the anisotropic solid-liquid interface and the blue and dotted line is the Read-Shockley grain boundary (independent on interface inclination).

2.2 Nucleation probability assessment

2.2.1 Problem statement

A polycrystalline film grows from a liquid parent phase. Nucleation during the film growth is expected, which then occurs on the same material, as is being deposited. In this system there are two distinct types of interfaces: the solid-liquid interface with inclination-dependent interface energy; and the grain boundary following the Read-Shockley dependence on misorientation (inclination-independent, though). Every grain has a particular crystallographic orientation (in 2D characterized by a single angle α). The grain orientation α coincides with the rotation of the solid-liquid interface energy anisotropy function (**??**).

A single nucleation event is always assumed to take place on a straight solid-liquid interface. The nucleus is assumed to take on an energy-minimizing equilibrium shape. Hence, in the case of multiple possible solutions, the one with the smallest area is selected.

A sketch of a single nucleation event is in Figure 2.1. The substrate is a plane, hence the orientation of its normal and the interface energy are equal on both sides of the particle. However, due to the problem geometry it is seen differently

in the polar coordinate systems associated with the left and right contact angle - the normal is $+\pi/2$ on the left and $-\pi/2$ on the right, hence $\sigma_1^L\left(\frac{\pi}{2}\right) = \sigma_1^R\left(-\frac{\pi}{2}\right)$.

Specifically, the solid-liquid interface energy is

$$\sigma_{SL}(\theta) = \sigma_{SL}^0 h(\theta)\,, \tag{2.9}$$

where $h(\theta)$ is the anisotropy function (**??**). The Read-Shockley grain boundary energy dependence is a function of disorientation $\Delta\alpha(\alpha_1, \alpha_2)$

$$\sigma_{GB}(\alpha_1, \alpha_2) = \begin{cases} \sigma_{GB}^0 \frac{\Delta\alpha(\alpha_1,\alpha_2)}{\Delta_{lim}} \ln\left(\frac{\Delta\alpha(\alpha_1,\alpha_2)}{\Delta_{lim}}\right) & \Delta\alpha \leq \Delta_{lim} \\ \sigma_{GB}^0 & \Delta\alpha > \Delta_{lim} \end{cases}, \tag{2.10}$$

with $\Delta_{lim} = 15°$ used here. Note that due to the problem symmetry of order n, the Read-Shockley dependence must be periodic too, hence the common disorientation definition $\Delta\alpha = |\alpha_1 - \alpha_2|$ cannot be used. The periodicity can be achieved using *modulo with rounded division convention* [13]

$$\Delta\alpha(\alpha_1, \alpha_2) = \mathrm{mod}(\alpha_1 - \alpha_2, 2\pi/n)\,, \tag{2.11}$$

where $\mathrm{mod}(x, y) = x - y\mathrm{round}(x/y)$. This way, the disorientation is always within $-\pi/n \leq \Delta\alpha \leq \pi/n$ and the minimum of Read-Shockley appears at $k\pi/n$, where $k = -1, 0, 1$.

The bottom grain orientation is α_1 and the nucleus orientation is α_2. The respective interface energies are expressed as

$$\sigma_1^L\left(\tfrac{\pi}{2}\right) = \sigma_1^R\left(-\tfrac{\pi}{2}\right) = \sigma_{SL}^0 h\left(\tfrac{\pi}{2} - \alpha_1\right) \tag{2.12}$$

$$\sigma_2(\theta_2) = \sigma_{SL}^0 h(\theta_2 - \alpha_2) \tag{2.13}$$

$$\sigma_3 = \sigma_{GB}(\alpha_1, \alpha_2)\,. \tag{2.14}$$

Then, the wetting parameter Γ can be expressed as a function of the bottom grain and nucleus orientations

$$\Gamma(\alpha_1, \alpha_2) = \frac{\sigma_1^L(\frac{\pi}{2}) - \sigma_3(\alpha_1, \alpha_2)}{\sigma_{SL}^0} \tag{2.15}$$

$$= h(\tfrac{\pi}{2} - \alpha_1) - \frac{\sigma_{GB}(\alpha_1, \alpha_2)}{\sigma_{SL}^0}\,. \tag{2.16}$$

It was assumed that $\sigma_{GB}^0 = \sigma_{SL}^0 = 0.3\,\mathrm{J/m^2}$.

With all above, the geometric problem is fully specified by the pair of orientations (α_1, α_2), both of which are from the interval $0 \leq \alpha < 2\pi/n$. The top grain orientation α_2 specifies the rotation of the equilibrium shape and the wetting parameter (2.16) specifies where the truncating line passes.

2.2.2 Stability as function of the bottom grain orientation

If the stability conditions (**??**) and (**??**) do not hold for either of the two contact angles, the shape is not stable. The condition (**??**) is fulfilled by default in the (generalized) Winterbottom construction. The condition (**??**) is simplified by the assumption of the grain boundary being inclination independent, because then $\tilde{\sigma}_3 = \sigma_3$. Using the interface stiffness definition (**??**) and the interface energies (2.12), (2.14), the condition (**??**) can be written

$$h(\tfrac{\pi}{2} - \alpha_1) + h''(\tfrac{\pi}{2} - \alpha_1) > -\frac{\sigma_{GB}(\alpha_1, \alpha_2)}{\sigma^0_{SL}}\,, \tag{2.17}$$

which holds for any twice-differentiable anisotropy function $h(\theta)$. Apparently, the right-hand side is always negative and it is the term $h''(\frac{\pi}{2} - \alpha_1)$, which decides the stability. As stated before, the interface stiffness is only negative for forbidden angles, around maxima of the anisotropy function. Hence, the above condition may be violated only when the substrate normal is aligned with a forbidden angle. This conclusion stems from the problem geometry and energetics, it is independent of the form of anisotropy function $h(\theta)$.

After substitution of (**??**) into (**??**) and rearrangement, the second condition becomes

$$\cos\left[n(\tfrac{\pi}{2} - \alpha_1)\right] < \frac{1}{\Omega}\left(\frac{\sigma_{GB}(\alpha_1, \alpha_2)}{\sigma^0_{SL}} + 1\right)\,. \tag{2.18}$$

The right-hand side is always positive. Apparently, when the right-hand side is greater than 1, the triple junction configuration is stable for any bottom grain orientation α_1. That certainly holds for weak anisotropies, i.e. when $\Omega \leq 1$. For stronger anisotropies $\Omega > 1$, the right-hand side may get smaller than 1 and some orientations α_1 then do not meet the stability condition. The stronger the anisotropy, the closer is the right-hand side to zero and the interval of unstable α_1 orientations is wider.

Effectively, the (3D) nucleation is blocked on high-energy crystal facets due to the strong anisotropy.

2.2.3 Shape factor-orientation maps

Here, the shape factor-orientation map is the 2D plot of the shape factor as function of the top and bottom grain orientation, i.e. $S(\alpha_1, \alpha_2)$. For isotropic nucleation, the solid-liquid interface had constant interface energy σ^0_{SL} and the grain boundary followed the Read-Shockley dependence (2.10).

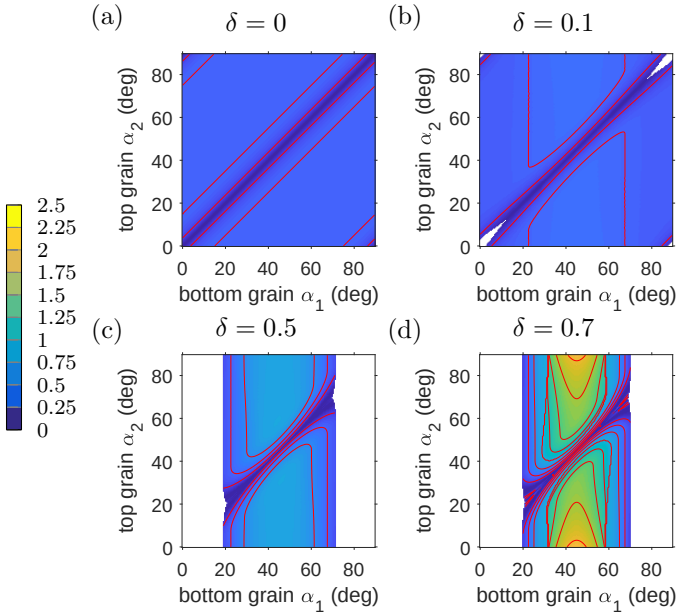

Figure 2.2: Shape factor-orientation maps for four different strengths of anisotropy in 4-fold symmetry (180x180 points). In (a) is the isotropic case, in (b)-(c) the anisotropic ones, the strength of anisotropy δ is indicated above. The white regions indicate the unstable orientations as by the condition (2.18). The levels are drawn with the increment of 0.25, like the colorbar spacing.

In anisotropic nucleation, the shape factor $S(\alpha_1, \alpha_2)$ was obtained from the generalized Winterbottom construction, with the wetting parameter $\Gamma(\alpha_1, \alpha_2)$ from (2.16). A solver was programmed in MATLAB, which found the possible solutions in the generalized Winterbottom construction and selected the one with the minimal area. It included all types of solutions discussed in this paper and it is available in Mendeley Data repository [8]. This solver was used to find $S(\alpha_1, \alpha_2)$ for all intended pairs of bottom and top grain orientations (α_1, α_2).

Examples of the shape factor-orientation maps $S(\alpha_1, \alpha_2)$ for four different strengths of anisotropy in 4-fold symmetry are shown in Figure 2.2.

In Figure 2.2a, there is the map for the case of a particle with isotropic solid-liquid interface energy. There, the shape factor can be analytically determined, because the isolated equilibrium shape is a circle. Hence, the heterogeneous nucleus shape is a circular segment and from the basic geometric relations one

can write

$$S = \frac{\phi - \sin(\phi)}{2\pi}\,, \tag{2.19}$$

where ϕ is the central angle of the circular segment, which relates to the wetting parameter Γ (2.16) simply as

$$\phi = 2\mathrm{acos}(\Gamma)\,. \tag{2.20}$$

Except for the regions of close orientations $\Delta\alpha \leq \Delta_{lim}$ (i.e. the diagonal and the corners of the map), there is constant $\Gamma = 0$, hence $\phi = \pi$ and $S = 0.5$ (i.e. the shape is a semicircle). For close orientations $\Delta\alpha \leq \Delta_{lim}$, the Read-Shockley grain boundary energy dependence implies smaller grain boundary energies (approaching 0 when the orientations are the same), which propagates through the equations for Γ, ϕ and eventually causes the drop of S to zero. That corresponds to wetting behavior (and larger nucleation probability).

The diagonal valley due to the misorientation dependence of the grain boundary energy is a feature common to all the maps.

Another common feature of the anisotropic maps in Figure 2.1b-d is that the low-energy bottom grain orientations (in the 4-fold case around $\alpha_1 \approx 45°$, see Figure 2.1b) are associated with larger values of the shape factor, i.e. with a rather de-wetting behavior, where the equilibrium shapes are rather emerged than submerged. As a result, the nucleation probability is lower on the low-energy planes. That is understandable, because such planes are in an energetically convenient configuration and the nucleation event would disturb that. Nevertheless, together with the nuclei instability on high-energy planes, it implies that there is no simple rule to foresee, where the nucleation is most likely.

Apparently, the landscape in the shape factor-orientation map is more hilly with stronger anisotropy. For $\delta = 0.7$ in Figure 2.2d there even are regions $S(\alpha_1, \alpha_2) > 1$.

In Figure 2.2b and c, all points in the map correspond to the basic solution of truncated isolated Wulff shape, but in Figure 2.2d there are also inverted shape and emerged Wulff solutions. This variability in solutions determines the more complex landscape.

These shape factor-orientations maps were used as input to the Monte Carlo simulation of growing polycrystalline film, described in the following section.

2.3 Monte Carlo simulations

The purpose of this section is to qualitatively demonstrate the possible impact of anisotropy in nucleation barrier due to anisotropic solid-liquid interface energy on the texture evolution during film growth and compare it to the case with isotropic solid-liquid interface energy. The shape factor-orientation maps were used together with a Monte Carlo simulation of growing 2D polycrystalline film.

One of the common microstructures observed in films deposited by various deposition techniques features V-shaped grains in columns (seen in the cross-section). That one occurs when the grain boundary has significantly lesser mobility than the advancing surface, and at the same time some grains have a growth advantage in the competition. It can be explained by either anisotropy in interface energy or in the growth rate [12].

There were two main requirements specifying the developed model. Firstly, it was to have the capability to simulate a columnar growth of polycrystalline film in 2D, where the total surface energy is minimized in time by favouring low-energy grains in the competition (i.e. interface-energy minimizing texture). Secondly, it should support inclusion of the nucleation with anisotropic interface energy as introduced in the preceding sections.

The used programme was written in MATLAB and is available in Mendeley Data repository [8].

In the following subsections are subsequently described: the Monte Carlo method itself, the methodology and the results.

2.3.1 Algorithm description

The Monte Carlo model was inspired by [4, 5], but significantly modified.

The simulation was carried out on a fixed square grid, where every node (or pixel, abbreviated px) had a value between 0-50. The value 0 represented the parent solution and 1-50 represented the crystalline solid of different crystallographic orientations from the interval $\langle 0, 2\pi/n)$. Each pixel could interact with its nearest and second nearest neighbors. The growth took place in the bottom-up direction, starting with a solid seed row, where random orientations were assigned to each pixel. In every column, there was one *growth site*, which was a liquid site having a solid neighbor on its bottom side, i.e. the first liquid site just above the deposit.

The simulation proceeded in iterations, one of which is described in a process

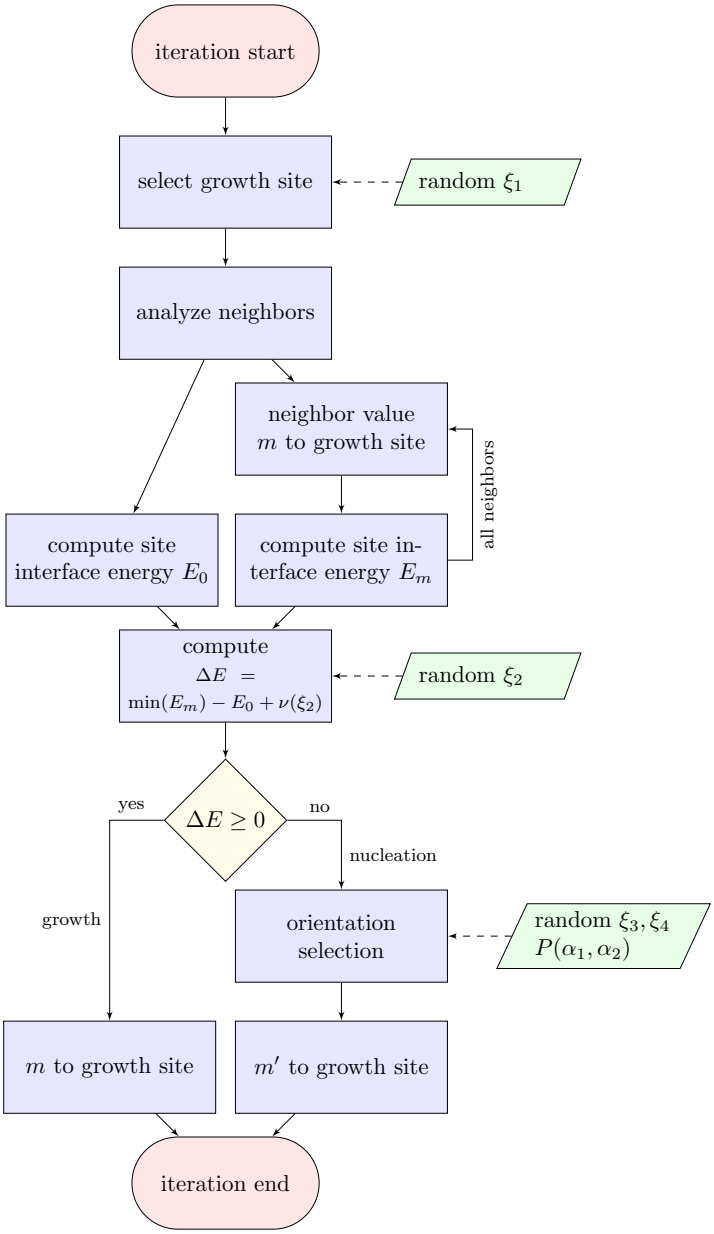

Figure 2.3: Process map of the Monte Carlo simulation with nucleation including anisotropic solid-liquid interface energy. In the model variant with no nucleation, the nucleation branch is omitted. In the model variant with isotropic nucleation, only ξ_3 is sampled and should the nucleation take place, the orientation is selected randomly.

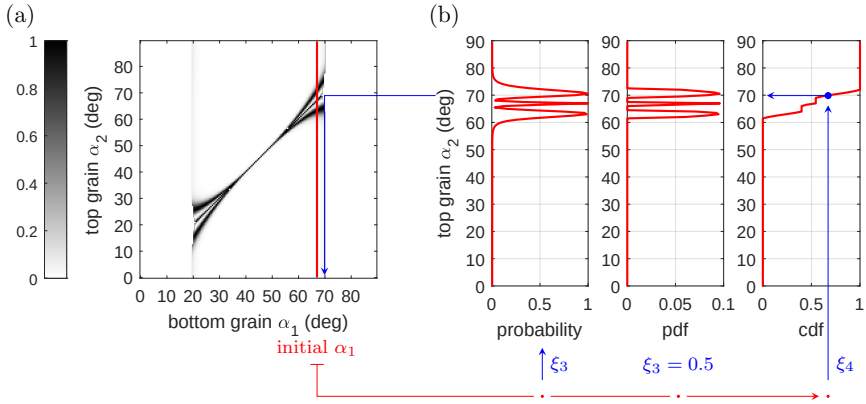

Figure 2.4: Single iteration of orientation selection algorithm. In (a) is the nucleation probability map $P(\alpha_1, \alpha_2) = \exp[(-10S(\alpha_1, \alpha_2)]$ for $n = 4$, $\delta = 0.7$. A slice at bottom grain orientation $\alpha_1 = 67°$ was indicated as the initial α_1. In (b) there is the respective slice of the probability map, from which the probability distribution function (pdf) and then the cumulative distribution function (cdf) of the top grain orientation are computed. The uniformly sampled ξ_3 is used in specification of the pdf (see text), here $\xi_3 = 0.5$ was used. Then, ξ_4 is used for sampling of the cdf to obtain the top grain orientation. The top grain orientation reached in this sampling is $\alpha_2 = 70°$.

chart in Figure 2.3. Essentially, a growth site was first selected, its neighborhood analyzed and then it was decided whether either some neighbor value would be inserted to the growth site (the *growth* branch in the scheme) or whether a nucleation attempt would take place (the *nucleation* branch). The latter could be omitted to produce only anisotropic growth without nucleation.

In the neighborhood analysis, the site interface energy E_0 was first computed for the initial case (when the growth site was occupied by the liquid) as

$$E_0 = \sigma_S(\alpha_1) = \sigma_{SL}^0 h\left(\tfrac{\pi}{2} - \alpha_1\right) . \tag{2.21}$$

As can be seen, the assumed surface orientation in every growth site was $\theta = \frac{\pi}{2}$ (the growth direction). In this sense, the deposit is assumed to be flat. Secondly, the site interface energies $E_{m''}$ were computed for all the neighbor orientations m''. In case of multiple different orientations m'' in the neighborhood, there would be multiple $E_{m''}$ site energies computed at this step as

$$E_{m''} = \sum_{i,nn} \sigma_i + w_{snn} \sum_{i,snn} \sigma_i + \sigma_S(\alpha_1) . \tag{2.22}$$

The symbol σ_i stands for the interface energy between the individual nearest neighbors (nn) or second nearest neighbors (snn). All the interfacial energies were taken positive. The second nearest neighbors were included with the weight $0 < w_{snn} < 1$ depending on the order of symmetry n. For 4-fold symmetry it was $w_{snn} = 1/4.4 = 0.2273$ (see 2.3.2 for details).

Upon replacement of liquid by solid there occurs an energy change ΔE, which was computed using the lowest site energy of all the available orientations m'', i.e.

$$\Delta E = \min(E_{m''}) - E_0 + \nu(\xi_2)\,, \tag{2.23}$$

where the noise term $\nu(\xi_2)$ represents local energy fluctuations and is commented in more detail below. As indicated in the scheme, when it was $\Delta E \geq 0$, the growth proceeded with the orientation m'' with the minimal site energy. On the other hand, when it was $\Delta E < 0$, the nucleation trial took place and the orientation was determined using the orientation selection algorithm described below.

In growing bicrystal simulations (without the nucleation) it was validated that such growth algorithm mimics the columnar growth with interface-energy-minimizing textures sufficiently for the purpose of this study. Details about the validation simulations are provided in the 2.3.2.

The noise term $\nu(\xi_2)$ was relevant for the nucleation. Every time the growth site was not near a grain boundary (i.e. there was only single neighbor orientation m''), the only possible interfacial energy change was strictly zero, i.e. $\Delta E = 0$. That was because the interface energy between like orientations was zero, hence in this case $E_{m''} = E_0$. This energy change corresponded to growth (see the scheme in Figure 2.3), hence no nucleation could occur in these sites. Generally speaking, the nucleation is certainly not limited only to the grain boundaries intersecting the surface. In order to enable nucleation everywhere on the surface, the fluctuations $\nu(\xi_2)$ were added.

In absolute value, they were so small, that they did not affect the result of local energies comparison near the grain boundaries (i.e. in growth sites with multiple orientations m'' in the neighborhood). At the same time, the fluctuations had a finite value attaining the minus sign with a controlled probability (when $\Delta E < 0$, the nucleation trial occurred instead of growth). Specifically, the fluctuations were taken as

$$\nu(\xi_2) = a(\xi_2 - b)\,, \tag{2.24}$$

where $a = 0.001\sigma_0$, $b = 0.25$ and $0 < \xi_2 < 1$ was sampled from the uniform distribution. Effectively, the parameter b controlled the density of nucleation attempts. With this particular parametrization, statistically every fourth growth site not adjacent to the grain boundary attempted to nucleate.

One nucleation attempt within the orientation selection algorithm is illustrated in Figure 2.4a-b. The orientation selection algorithm determined two things: i) whether anything nucleated and ii) with which orientation. Depending on the bottom grain orientation, there is a certain probability distribution for the top grain (nucleus) orientations, which derives from the nucleation probability map (see Figure 2.4a)

$$P(\alpha_1, \alpha_2) = \exp[-\beta S(\alpha_1, \alpha_2)]\,. \tag{2.25}$$

Should a random number drawn from uniform distribution be lower than the nucleation probability $P(\alpha_1, \alpha_2)$, the event takes place. This is the random number ξ_3 in the scheme in Figures 2.3 and 2.4. But after such sampling there possibly are multiple top grain orientations which could occur, i.e. such orientations α_2' that $P(\alpha_2') > \xi_3$ for given α_1. Hence such probability density function (pdf) is used, which assigns zero nucleation probability to all α_2 orientations except for those α_2's. After computation of the corresponding cumulative distribution function (cdf), the top grain orientation can be sampled from the pdf created in the previous step (using random ξ_4 sampled from uniform distribution), as illustrated in Figure 2.4b.

Result of this iteration was either a new grain orientation or unsuccessful nucleation - that happened when the sampled $\xi_3 > P(\alpha_2)$ for all α_2 in the respective slice of the probability map. The growth site then remained liquid. Note though, that this was very unlikely for the demonstrative iteration in Figure 2.4, because it corresponds to high anisotropy and low nucleation barrier, which are strongly nucleation-favoring conditions. In general, however, the nucleation does not occur automatically, as can be seen in Figure 2.6, where the mean number of nucleation events clearly depends on the nucleation barrier β and the strength of anisotropy δ.

2.3.2 Validation of anisotropic growth

Let a planar surface in 3D be intersected by a grain boundary between two crystals with different surface energies. The in-plane capillary force acting on the triple junction line is equal to the difference in the respective surface energies and is independent of the anisotropic torque term [3].

The simulated bicrystal consisted of the maximum- and minimum-energy orientation for a given strength of anisotropy δ. With the anisotropy function (**??**) the maximal surface energy was thus $\sigma_{max} = \sigma_0(1 + \delta)$ and the minimal one $\sigma_{min} = \sigma_0(1 - \delta)$. The magnitude of in-plane force F_x on the junction is then

$$|F_x| = 2\sigma_0\delta\,. \tag{2.26}$$

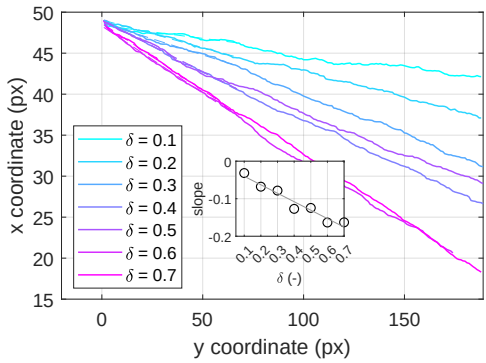

Figure 2.5: Mean trajectory of a triple point on the bicrystal surface during simulated growth for different strengths of anisotropy δ. The mean was taken from 30 runs in a system 100x200 px. The inset shows the slope of the trajectories and demonstrates that the greater was the anisotropy, the greater was he drag.

The sign of F_x is such to expand the low-energy half-plane on the expense of the high-energy one.

The simulations were carried out for a range of strengths of anisotropy δ. The second-nearest neighbor weight w_{snn} from (2.22) was optimized to observe a linear trend in the slope of the triple point trajectory during the simulation. There were always made 30 runs in a system 100x200 and the mean path was fitted by a straight line. The weight $w_{snn} = 1/4.4$ produced the trajectories as in the Figure 2.5. In the inset of this figure, the slopes were plotted as function of δ and the trend is certainly sufficiently linear for a qualitative study in this paper.

2.3.3 Methodology

In this study, three deposition scenarios were compared:

1. No nucleation (NN) - only anisotropic growth.
2. Isotropic nucleation (IN) - $S(\alpha_1, \alpha_2)$ as in Figure 2.2a.
3. Anisotropic nucleation (AN) - $S(\alpha_1, \alpha_2)$ as obtained by the generalized Winterbottom construction, e.g. like in Figure 2.2b-d. 4-fold symmetry was assumed.

Parameter	Values	Total
nucleation scenario	NN, IN, AN	3
initial condition	IC_A, IC_L, IC_H	3
strength of anisotropy δ	0.1, 0.3, 0.5, 0.7	4
non-dim. nucl. barrier β	10, (30), 50, 90	3 (4)

Table 2.1: Simulation conditions included in this study. Simulations at all combinations of the above parameters were run (except for those in parenthesis, which were combined only with some). In total, there were 116 simulation runs differing in these parameter combinations.

Because in the the anisotropic nucleation, the nucleation probability is a function of the bottom grain orientation, its manifestation depends on the initial texture, i.e. on the seed layer orientation distribution. For this reason, tree different initial conditions were investigated, where the orientations were always drawn from uniform distribution, but from different domains:

1. IC_A: sampled from $\langle 0, 1)\frac{2\pi}{n}$, i.e. all orientations (theoretically, a deposition on amorphous substrate),
2. IC_L: sampled from $\langle 0.2, 0.8\rangle\frac{2\pi}{n}$, i.e. in 4-fold symmetry centered around low-energy orientations ,
3. IC_H: sampled from $[\langle 0, 0.3\rangle \cup \langle 0.7, 1)]\frac{2\pi}{n}$, i.e. in 4-fold symmetry centered around high-energy orientations.

The individual pixels in the seed layer were sampled independently, i.e. the intended grain size is 1 px. The conditions IC_H and IC_L both sample from the interval of orientations of width $0.6\frac{2\pi}{n}$, which is wide enough to include at least part of both stable and unstable regions in both the conditions.

Additionally, the strength of anisotropy δ and the non-dimensional nucleation barrier β were varied. Specifically, all the different parameter values are summarized in Table 2.1.

A single simulation run took place in a rectangular system on a grid 1500x200. In order to gain better statistics on the through-thickness orientation evolution and the nucleation behavior, 10 repetitions were carried out and the results were either averaged or interpreted from one pseudo system 15000x200.

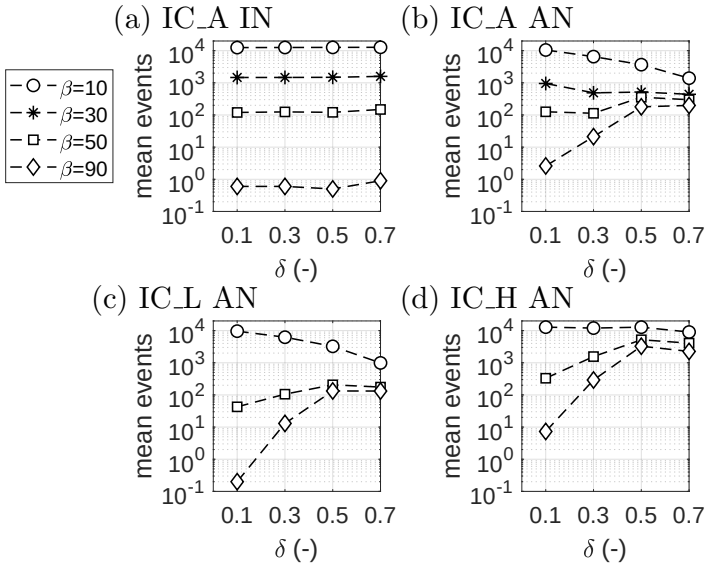

Figure 2.6: Mean number of nucleation events per single simulation run in the system 1500x200 for different initial conditions. The legend is common to all graphs, which all correspond to $n = 4, \delta = 0.5$. IC_A, IC_L and IC_H are the initial conditions (all orientations, low-energy orientations only and high-energy orientations only, respectively). IN and AN stand for the nucleation with isotropic and anisotropic solid-liquid interface energy, respectively.

2.3.4 Results

The presented results are based on analysis of 116 simulation runs, differing in the parameter combinations from Table 2.1.

In Figure 2.6, there is the mean of nucleation events (averaged over ten 1500x200 simulations) as a function of strength of anisotropy δ in series of nucleation barrier β and at different initial conditions. Figure 2.6a shows the result at initial condition IC_A, isotropic nucleation. In isotropic nucleation, the number of nucleation events was only dependent on the nucleation barrier β, not on the strength of anisotropy nor on the initial condition. Figure 2.6b shows the same initial condition (IC_A), but anisotropic nucleation. There, the number of nucleation events depends on both the strength of anisotropy δ and the nucleation barrier β. At small anisotropy, the dependence of mean events on β is similar to the isotropic nucleation. With increasing the strength of anisotropy, there is weaker dependence on β. It was observed, that even at otherwise

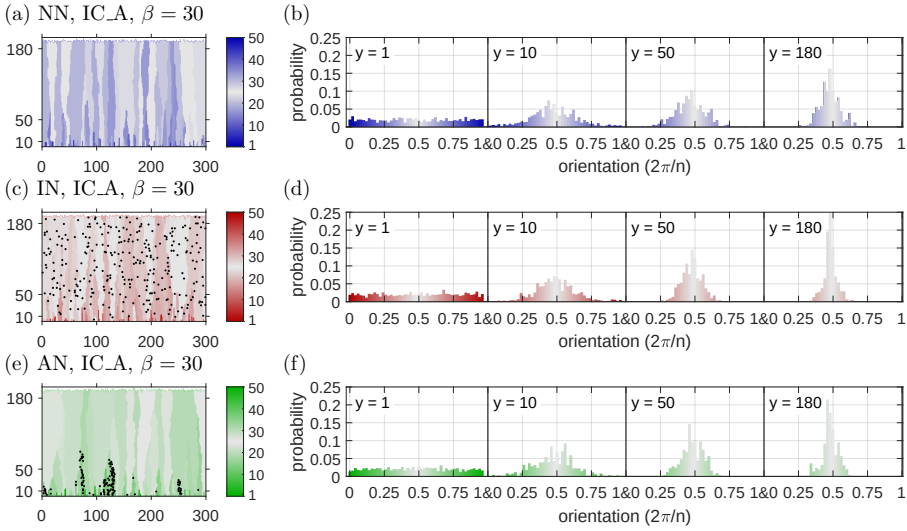

Figure 2.7: Deposits and their texture evolution in different nucleation scenarios and the initial condition IC_A, $\delta = 0.5$, $n = 4$ and $\beta = 30$. In (a), (b) is the no-nucleation scenario, in (c), (d) is isotropic nucleation and in (e), (f) is the anisotropic nucleation. In (a), (c) and (e) are the deposits, with the nucleation events indicated by black dots, and in (b), (d), (f) are the histograms of orientations in the indicated rows of the deposits. Light gray always corresponds to the low-energy orientations in both the deposits and histograms and the high-energy orientations are correspondingly color-coded in both plots of the same scenario.

prohibitively small nucleation barrier $\beta = 90$, hundreds of nucleation events occurred in the 1500x200 system for $\delta \geq 0.5$ and remained rather constant after increase to $\delta = 0.7$. On the other hand, at very low nucleation barrier $\beta = 10$, the mean events were decreasing when δ rose, approaching the same order of magnitude like in large nucleation barriers β. In Figure 2.6c, again the anisotropic nucleation is shown, now in the initial condition IC_L. With the seed layer bias towards low-energy orientations, the results are very similar to those in Figure 2.6b, only the numbers are slightly smaller. Larger difference was observed in Figure 2.6d, initial condition IC_H, anisotropic nucleation. With the seed layer centered around high-energy orientations, $10^3 - 10^4$ of events were observed even at very high nucleation barrier $\beta = 90$ for $\delta \geq 0.5$.

Figure 2.7 presents the resulting deposits and their texture evolution in the three deposition scenarios in IC_A at $\delta = 0.5$ and $\beta = 30$. The no-nucleation scenario in Figure 2.7a-b shows the bias towards the low-energy orientations

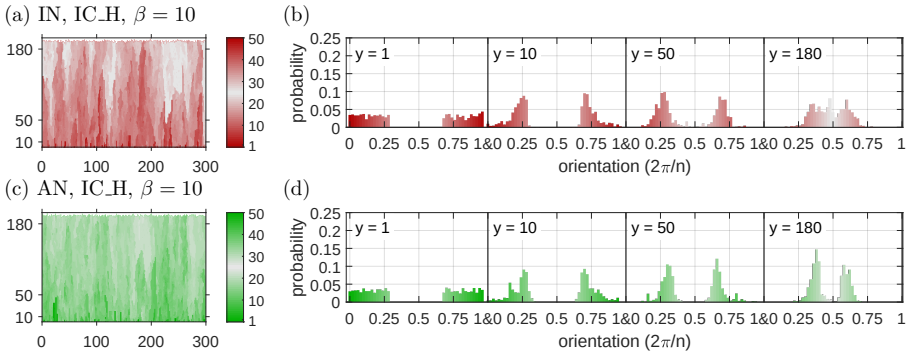

Figure 2.8: Deposits and their texture evolution in different nucleation scenarios and initial condition IC_H, $\delta = 0.5$ and $\beta = 10$. In (a), (b) is the isotropic nucleation scenario, in (c), (d) is anisotropic nucleation. The nucleation events are not shown, because they were too many. See caption of Figure 2.7 and the text for more details.

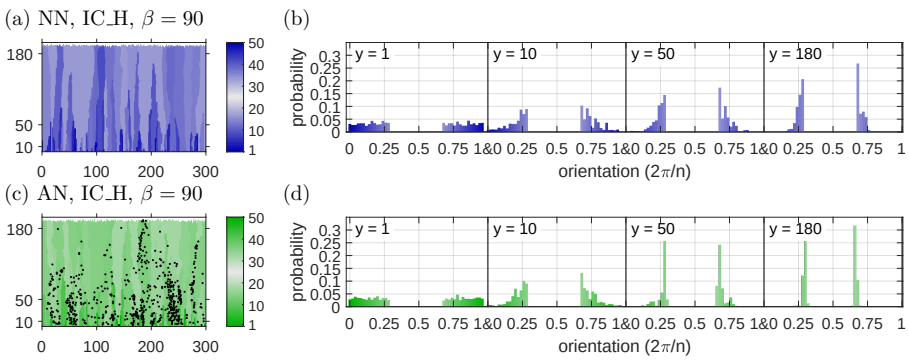

Figure 2.9: Deposits and their texture evolution in different nucleation scenarios and initial condition IC_H, $\delta = 0.5, n = 4$ and $\beta = 90$. In (a), (b) is the no-nucleation scenario, in (c), (d) is anisotropic nucleation. See caption of Figure 2.7 and the text for more details.

in the middle of the interval $(0, 1)\frac{2\pi}{4}$ with increasing film thickness. this is the desired and a characteristic feature of the model. All three deposition scenarios exhibit the columnar microstructure.

At this nucleation barrier β and initial condition, the mean number of nucleation events was comparable in the isotropic and anisotropic nucleation (see Figures 2.6a-b at $\delta = 0.5$). At first sight, the biggest difference between the isotropic and anisotropic nucleation scenarios is the spatial distribution of the nucleation events. While in the isotropic case (Figure 2.7c) the nucleation was uniform, in the anisotropic one (Figure 2.7e) it is clearly located only at specific grains, which were apparently favourably oriented for nucleation. There, nucleation occurred densely. This is mainly attributed to two factors: i) the stability condition prohibits nucleation on too high-energy-interface grains and ii) nucleation on the lowest-energy planes is the least probable of the allowed ones (and with strong enough anisotropy practically prohibited as well). Eventually, the nucleation took place on the bottom grain orientations near the edges of the stable orientations region, where the shape factor is closer to zero (see the map in Figure 2.2c, where it is also $\delta = 0.5$). The (nucleated) top grain orientation will mostly be close to the bottom grain orientation. The effect of nucleation on texture is such that the low-energy orientation texture is stronger near the film surface. This is probably because nucleation introduces single-pixel orientation inhomogeneities, which are easy for neighboring lower-energy grains to overgrow. The different spatial distribution of events in the isotropic and anisotropic nucleation scenarios affects the texture in the same way - i.e. in this case a mild increase in strength of the low-interface-energy texture.

On the other hand, the textures of scenarios with nucleation were not recognizable from the no-nucleation scenario when the mean number of events per simulation was in the order of magnitude 10^2 and smaller. In the initial condition IC_A, some effect is noticeable with 10^3 events per simulation (as in Figure 2.7) and above. Apparently, the effect of nucleation on texture will be stronger with more events taking place.

An example of deposits and texture evolution at high nucleation rate at $\beta = 10$ in isotropic and anisotropic nucleation scenario is in Figure 2.8 (as before, $\delta = 0.5, n = 4$). Note that the initial condition is IC_H, where the low-energy orientations are absent. Again, the mean number of nucleation events are comparable in the two scenarios. In the isotropic nucleation scenario (Figure 2.8a-b), some low-energy grains are eventually inserted (with equal probability as any other) and these would overtake given enough film thickness. Below the film surface (row 180, Figure 2.8b), the texture is already centered around the low-energy orientations with rather uniform distribution. On the other hand, in the anisotropic nucleation scenario (Figure 2.8c-d), the nucleation of low-energy grain is apparently much less likely than of other orientations.

This delays the introduction of the interface energy minimizing texture, as can be seen in Figure 2.8d, row 180, where the central minimum-energy orientations are still missing.

The anisotropic nature of nucleation thus imposed a different than interface energy minimizing texture, which is a very interesting observation. Note that the probability of minimum-energy grain insertion is non-zero, so in principle the interface-energy-minimizing texture under the surface is the expected terminal state. However, depending on the anisotropy and other conditions it may as well be unlikely within the practical deposition thicknesses.

Figure 2.9 presents the case of very high nucleation barrier $\beta = 90$, again in the initial condition IC_H (and $\delta = 0.5$, $n = 4$). There occurs nearly no nucleation in the isotropic nucleation scenario (on average less than 1 event per simulation), so it is identical to the no-nucleation scenario (shown in Figure 2.9a-b). As can be seen, the lowest-available-energy grains overtake as before, but there is no mechanism to introduce orientations absent in the seed layer. In the anisotropic nucleation scenario (Figure 2.9c-d), still about 10^3 of nucleation events took place despite the very high nucleation barrier β. That was possible because of she shape factor anisotropy - the local nucleation barrier $S(\alpha_1, \alpha_2)\beta$ was small enough for some orientations. However, the introduction of low-energy orientations did not take place, so the nucleation only supported the grains with initially-present lowest interface energy in the growth competition,

2.4 Comparison to experiment and discussion

The presented theory can be used to qualitatively explain some recent experimental results by Alimadadi et al. [1]. They studied the through-thickness texture evolution in Ni electrodeposited on amorphous substrate in four samples, each of which exhibited different dominant fiber texture. The only variables in the deposition were pH and deposition rate, the resulting thickness was different in every sample, but around 20 µm.

The sample deposited at the smallest rate of 0.533 nm/s (i.e. an order of magnitude smaller than the others, the current density being $0.2\,\mathrm{A/dm^2}$) exhibited sudden change of texture in the low thickness of 0-4 µm, as can be seen in Figure 2.10. The $\langle 100 \rangle$ texture in the nanocrystalline zone A below the 2 µm of thickness is gone in the pole figure of 2-4 µm, where the $\langle 110 \rangle$ component starts developing and later strenghtens with increasing thickness. Very few grains reaching the surface could be traced back to the nanocrystalline zone A, which means that nucleation had to take place [1]. The nucleation was apparently anisotropic (with a bias towards $\langle 110 \rangle$). The combination of nuclei

density and their advantage in growth was able to set a completely new course to the texture evolution within a rather thin layer of the deposit.

In the other samples of Alimadadi, the initial texture contained the resulting dominant component, which gradually reinforced with thickness (similarly to how the sample in Figure 2.10 evolved from 2 µm on).

Interestingly, the nucleation in the discussed sample happened at very low growth rate, which in general implies high nucleation barriers. The nucleation barrier for the emerging nuclei had to be very small, though, because the nucleation took place regardless of the small driving force. The possibility of low nucleation barrier even with low driving force (given a convenient bottom grain orientation) was shown to be one of possible manifestations of anisotropic nucleation barrier (see Figure 2.9).

Detailed analysis of the possible competition between the interface-energy-minimization and strain-energy-minimization mechanisms of texture formation in this case is out of the scope of this paper. The sole fact that significant amount of anisotropic, growth-successful nuclei appeared at very low driving force is a peculiarity, which can be qualitatively explained by the presented results, though.

Possibly one mechanism sustained the texture by setting the rules for growth competition up to certain thickness. With the overtake of the other mechanism then, possibly the nuclei would suddenly have more chances in the growth competition. At the same time, the initial favourable-for-nucleation texture would still be in place, before overgrown by the nuclei.

An attempt to estimate the non-dimensional nucleation barrier β in the discussed experiment was made. However, with so small driving force, the effect of the (unknown) scaling interface energy σ_0 on the nucleation barrier is very large. The non-dimensional nucleation barrier β in multiples of kT then varied between 3 and 2950 for σ_0 equal to 0.1 and $1\,\mathrm{J/m^2}$, respectively. The actual value of σ_0 cannot be reached, but if the nucleation barrier was so small due to the low σ_0, a very high nucleation rate would be expected during the whole experiment. It would not explain the observed sudden change in the texture (supposedly due to nucleation) and the long columnar grains seen in this sample (see Figure 2.10) should not occur at all.

Alimadadi et. al [1] did not investigate in depth what mechanisms were responsible for the texture change in this sample. The hereby presented interpretation is extending their discussion and there are no points of disagreement.

Should the anisotropy function produce Wulff shape with facets, there would

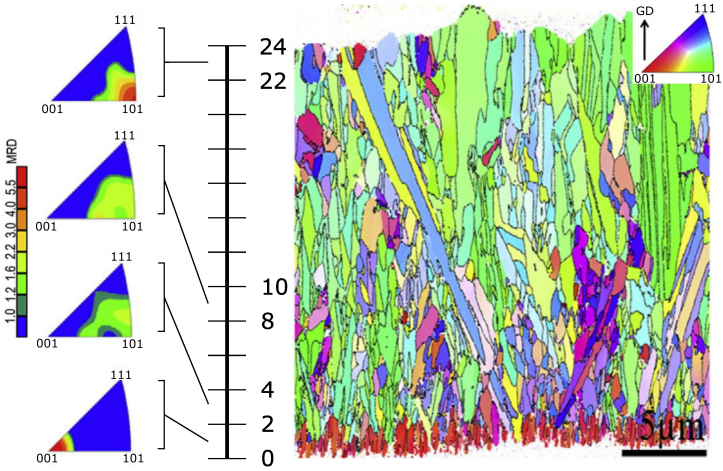

Figure 2.10: Experimental results of Ni electrodeposited on an amorphous substrate, adapted from [1]. On the right, an EBSD map of the deposit cross-section is shown, the inverse pole figure is in the top-right inset. The axis indicates the deposit thickness in µm. The pole figures on the left correspond to the indicated regions, their colorbar of MRD (Multiples of Random Distribution) is provided.

be no self-intersection of the Wulff plot, because that one is formed essentially by single orientation per facet. However, in such shapes, nearly all orientations are forbidden, i.e. with negative interface stiffness. We remind that not all the forbidden orientations are to fail the stability condition (2.17), but they are the candidates for doing so. The stability condition thus has possibly large implications for anisotropic nucleation in 2D space in general.

2.5 Conclusion

This chapter investigated implications of the anisotropy in interface energy for orientation selection in repeated nucleation during polycrystal deposition.

First, the wetting parameter Γ was expressed as a function of the top and bottom grain orientations in order to enable the generalized Winterbottom construction for each orientation combination. Novel solutions to the stable equilibrium shape were employed in very strong anisotropies. The shape factor-orientation maps were produced and used as input to the columnar growth simulation using the developed Monte Carlo method.

The obtained results essentially indicate that with stronger anisotropy, there is less effect of the non-dimensional homogeneous nucleation barrier on the nucleation rate. In a system with constant scalar interface energy σ_0 and temperature, that means lesser effect of the bulk driving force on nucleation behavior (see (2.6)).

On the other hand, the initial texture becomes significant or even leading factor. Depending on the initial texture, it was shown to be possible to either have no nucleation irrespective of the driving force (should the initial texture contain only forbidden orientations) or to have large nucleation rate even with very small driving forces. The latter option was speculated to be one of mechanisms leading the abrupt change in texture in one of samples in [1], the one shown in Figure 2.10 in this paper.

Three improvements of the generalized Winterbottom construction were worked out: (i) the new solutions of stable equilibrium shapes, originating from multiple self-intersecting Wulff plot occurring at very strong ansiotropies, (ii) detailed description of the inverted shape solution in arbitrary orientation and (iii) the contact point stability condition for the nucleus as a function of both the top and bottom grain orientations. The latter is a strong influence on the model behavior. It masked the full orientation-shape factor map only to its part, where the nucleation is less probable, except for some areas near the edge of the stable angles interval. There, on the other hand, the nucleation barrier could be so small, that nucleation would proceed as well at very low driving forces.

The used MATLAB codes are available in a Mendeley Data repository [8].

Bibliography

[1] H. Alimadadi, A. B. Fanta, T. Kasama, M. A. Somers, and K. Pantleon. "Texture and microstructure evolution in nickel electrodeposited from an additive-free Watts electrolyte". In: *Surface and Coatings Technology* 299 (Aug. 2016), pp. 1–6. ISSN: 02578972. DOI: 10.1016/j.surfcoat.2016.04.068.

[2] S. Daubner, P. W. Hoffrogge, M. Minar, and B. Nestler. "Triple junction benchmark for multiphase-field and multi-order parameter models". In: *Computational Materials Science* 219 (Feb. 2023). ISSN: 09270256. DOI: 10.1016/j.commatsci.2022.111995.

[3] D. W. Hoffman and J. W. Cahn. "A vector thermodynamics for anisotropic surfaces. I. Fundamentals and application to plane surface junctions". In: *Surface Science* 31.C (1972), pp. 368–388. ISSN: 00396028. DOI: 10.1016/0039-6028(72)90268-3.

[4] D. Li and J. Szpunar. "A Monte Carlo simulation approach to the texture formation during electrodeposition—I. The simulation model". In: *Electrochimica Acta* 42 (1 Jan. 1997), pp. 37–45. ISSN: 00134686. DOI: 10.1016/0013-4686(96)00164-8.

[5] D. Li and J. Szpunar. "A Monte Carlo simulation approach to the texture formation during electrodeposition—II. Simulation and experiment". In: *Electrochimica Acta* 42 (1 Jan. 1997), pp. 47–60. ISSN: 00134686. DOI: 10.1016/0013-4686(96)00158-2.

[6] A. Mariaux and M. Rappaz. "Influence of anisotropy on heterogeneous nucleation". In: *Acta Materialia* 59 (3 2011), pp. 927–933. ISSN: 1359-6454. DOI: 10.1016/j.actamat.2010.10.015.

[7] A. Milchev. *Electrocrystallization: fundamentals of nucleation and growth.* Kluwer Academic Publishers, 2002. ISBN: 1-4020-7090-X. DOI: 10.1007/b113784.

[8] M. Minar. "Influence of surface energy anisotropy on nucleation and crystallographic texture of polycrystalline deposits". In: *Mendeley Data, v1* (2023). DOI: 10.17632/bsdff8shbz.1.

[9] M. Minar and N. Moelans. "Benchmarking of different strategies to include anisotropy in a curvature-driven multi-phase-field model". In: *Physical Review Materials* 6 (10 Oct. 2022), p. 103404. ISSN: 2475-9953. DOI: 10.1103/PhysRevMaterials.6.103404. URL: https://link.aps.org/doi/10.1103/PhysRevMaterials.6.103404.

[10] M. Minar and N. Moelans. "Influence of surface energy anisotropy on nucleation and crystallographic texture of polycrystalline deposits". In: *Computational Materials Science* 231 (Jan. 2024), p. 112575. ISSN: 0927-0256. DOI: 10.1016/J.COMMATSCI.2023.112575. URL: https://www.sciencedirect.com/science/article/abs/pii/S0927025623005694.

[11] D. A. Porter, K. E. Easterling, and K. E. Easterling. *Phase Transformations in Metals and Alloys (Revised Reprint)*. third. CRC Press, Feb. 2009. ISBN: 9780429112256. DOI: 10.1201/9781439883570. URL: https://www.taylorfrancis.com/books/9781439883570.

[12] F. Wendler, C. Mennerich, and B. Nestler. "A phase-field model for polycrystalline thin film growth". In: *Journal of Crystal Growth* 327.1 (2011), pp. 189–201. ISSN: 00220248. DOI: 10.1016/j.jcrysgro.2011.04.044. URL: http://dx.doi.org/10.1016/j.jcrysgro.2011.04.044.

[13] Wikipedia. *Modulo*. 2023. (Visited on 05/11/2023).

List of publications

First-author publications

[9] Minar, M., Moelans, N. (2022). Benchmarking of different strategies to include anisotropy in a curvature-driven multi-phase-field model. Physical Review Materials, 6(10), 103404.
https://doi.org/10.1103/PhysRevMaterials.6.103404

[10] Minar, M., Moelans, N. (2024). Influence of surface energy anisotropy on nucleation and crystallographic texture of polycrystalline deposits. Computational Materials Science, 231, 112575.
https://doi.org/10.1016/J.COMMATSCI.2023.112575

Collaborations

[2] Daubner, S., Hoffrogge, P. W., Minar, M., Nestler, B. (2023). Triple junction benchmark for multiphase-field and multi-order parameter models. Computational Materials Science, 219, 111995.
https://doi.org/10.1016/J.COMMATSCI.2022.111995